JGR Solid Earth

RESEARCH ARTICLE
10.1029/2019JB019169

Hydraulic Injection-Induced Velocity Changes Revealed by Surface Wave Coda and Polarization Data at a Shale Play Site in Southwest China

Yan Zhang[1,2], Fenglin Niu[2,3], Kai Tao[3], Jieyuan Ning[1], Haichao Chen[3], and Youcai Tang[3]

[1]Institute of Theoretical and Applied Geophysics, Peking University, Beijing, China, [2]Department of Earth, Environmental and Planetary Sciences, William Marsh Rice University, Houston, TX, USA, [3]State Key Laboratory of Petroleum Resources and Prospecting and Unconventional Petroleum Research Institute, China University of Petroleum at Beijing, Beijing, China

Abstract We investigated temporal variations of seismic wave velocity associated with hydraulic fracturing using Green's functions computed from ambient noise data. In October and November of 2014, we set up a broadband array at a shale play site inside the Sichuan basin where a pilot horizontal drilling and hydraulic injections were conducted. We first computed cross-correlation functions using continuous data recorded by 21 three-component broadband sensors deployed around the treatment well. We then employed a running window correlation-based coda wave interferometry technique to measure apparent velocity changes from the daily Green's functions of all the station pairs in the frequency range of 1 to 3 Hz. We found significant velocity changes right after the hydraulic fracturing, which exhibited a clear direction-dependent pattern. *S* wave velocity along raypaths parallel to the well trajectory showed a clear increase while those perpendicular exhibited a small decrease. The anisotropic changes in seismic velocity observed here were also confirmed from surface wave horizontal particle motion data. By comparing our observations with normal stress changes calculated with a half-space elastic model, we speculate that stress changes induced by the hydraulic fracturing were likely to be responsible for the observed anisotropic changes in seismic velocity. Our results suggest that time-lapse seismic imaging with ambient noise data provides a promising probe for monitoring geomechanical changes related to exploitation of unconventional oil and gas resources.

Key Points:
- Coda wave interferometry measurements from noise records of a monitoring broadband array showed a clear fracturing-related change
- Analysis of surface wave polarization directions revealed an azimuthal-anisotropy-induced periodic deviation in propagation direction
- Both the coda wave and polarization data indicated direction-dependent changes in seismic velocity caused by hydraulic injection

Supporting Information:
- Supporting Information S1

Correspondence to:
Y. Zhang,
zyzhangyan@pku.edu.cn

Citation:
Zhang, Y., Niu, F., Tao, K., Ning, J., Chen, H., & Tang, Y. (2020). Hydraulic injection-induced velocity changes revealed by surface wave coda and polarization data at a shale play site in southwest China. *Journal of Geophysical Research: Solid Earth*, *125*, e2019JB019169. https://doi.org/10.1029/2019JB019169

Received 6 DEC 2019
Accepted 9 SEP 2020
Accepted article online 16 SEP 2020

1. Introduction

Hydraulic fracturing is one of the key techniques employed by the energy industry to enhance rock permeability and reservoir drainage to efficiently exploit an unconventional hydrocarbon reservoir. Tens of thousands of cubic meters of water and thousands tons of sand are injected into the reservoir to create a connected fracture network, which induces large numbers of microseismic events of low magnitude (Warpinski et al., 2014). The microseismic events are commonly used to determine fracture geometry and to confine the so-called stimulated reservoir volume (SRV) of the hydraulic treatment (Chen et al., 2018; Maxwell et al., 2010). The large volume injection and the created fractures are likely to directly alter reservoir structure, resulting in significant changes in seismic properties of the reservoir, such as velocity, attenuation, and anisotropy, which have been shown by active source time-lapse (4-D) seismic imaging (e.g., Byerley et al., 2018; Meek et al., 2017).

Hydraulic injection is also expected to change the subsurface stress state in the reservoir and the surroundings, including the overburden rock. Many laboratory studies indicated that seismic velocities of crustal rocks change slightly with the stress level they are subjected to at low confining pressure (e.g., Birch, 1960; Nur & Simmons, 1969; Scholz, 1968). Such dependence is attributed to the opening/closing of microcracks due to changes in the stress normal to the crack surface. The measured velocity-stress sensitivity, which is defined as $\eta = dlnV/dP$ (Silver et al., 2007), where $dlnV$ and dP are perturbations of fractional velocity and confining pressure, varies from 10^{-7} to 10^{-9} Pa^{-1} depending on the crack density, which decreases rapidly with depth. If the injection-induced stress changes are in the range of tens to hundreds of kilopascals within the reservoir overburden, then we would expect measurable velocity changes even at the surface. Indeed, repeated active

source experiments indicated that similar path *P* waves traveling through the overburden above compacting reservoirs at the Ekofisk Field of the North Sea showed clear differences in travel time (Guilbot & Smith, 2002). Reservoir geomechanical modeling (Herwanger & Horne, 2009) suggested that injection and production induced stress change can lead to anisotropic deformation of the reservoir and surrounding rock, which is likely to cause direction-dependent changes in seismic velocity and attributes. Angerer et al. (2000) observed a 10% change in shear wave anisotropy from a 4-D three-component (3C) survey recorded before and after CO_2 injection in a fractured dolomite reservoir in Vacuum Field, New Mexico.

Most 4-D seismic imaging conducted by the energy industry used at least two active source datasets acquired by similar source-receiver configuration at different times. The repeating data acquisition is the key to ensure that any observed changes in seismic data from different surveys reflect changes in the medium, rather than changes associated with source or receiver configurations. Recently, continuous records of ambient noise have become effective sources to monitor temporal changes of the subsurface velocity field (e.g., Brenguier et al., 2008, 2014; Cheng et al., 2010; Obermann et al., 2013; Sens-Schönfelder & Larose, 2010). The ambient noise field can be largely approximated by a diffuse field, and the Green's function between two seismic stations can be obtained from the cross correlation of the field (e.g., Lobkis & Weaver, 2001; Shapiro et al., 2005; Snieder, 2004). Many ambient noise studies based on ballistic or coda surface waves have revealed significant temporal changes of seismic velocities associated with the occurrence of earthquakes (Brenguier et al., 2014; Cheng et al., 2010; Froment et al., 2013), volcanic deformation (Brenguier et al., 2008; Sens-Schönfelder & Wegler, 2006), and various nontectonic processes such as precipitation, thermoelastic strain, and reservoir exploitation (Chen et al., 2014; Hillers, Ben-Zion, et al., 2015; Hillers, Husen, et al., 2015; Hillers et al., 2020; Lecocq et al., 2017; Meier et al., 2010; Obermann et al., 2015; Sánchez-Pastor et al., 2019).

While it is less frequently used in 4-D seismic imaging by the oil and gas industry, the ambient noise-based techniques have been demonstrated to be capable to identify velocity changes within the overburden of reservoirs at various oil fields induced by hydraulic injection and hydrocarbon production (Corciulo, Roux, Campillo, & Dubucq, 2012; Delatre & Manceau, 2013; De Ridder & Biondi, 2013; Mordret et al., 2014). Corciulo, Roux, Campillo, Dubucq, et al. (2012) developed an instantaneous phase variation technique and applied it to a dense geophone array installed over an ~0.8-km-sided square area above an oil and gas exploration field. The measured relative velocity variations ($\delta v/v$) ranged from −0.15% to 0.1% over a 5-day period, which were speculated to be related to the ongoing production activities. It was, however, unclear how velocity perturbations were distributed within the square area and whether the observed velocity perturbations were caused by direct structural alteration or induced by stress changes. Mordret et al. (2014) computed Green's functions using ambient noise data recorded by the dense Valhall Life of the Field Seismic network with 2,320 sensors in the North Sea in two different periods, 2004 and 2005. For each station pair, they further obtained velocity changes from the ballistic surface waves computed from the 2004 and 2005 records. Finally, they applied the eikonal tomography and obtained lateral variation map of $\delta v/v$, which clearly showed a velocity increase of up to 0.08% in the southern part of the overburden. The velocity increase was attributed to the exploitation in the southern flank of the Valhall reservoir. If the subsurface stress field caused this increase, then it is likely that this part of the overburden underwent compression between 2004 and 2005.

Tanimoto (2004) showed that surface waves propagating in an azimuthally anisotropic medium are expected to have nonlinear horizontal particle motions with azimuth-dependent polarization directions. Numerical investigation of Saade et al. (2015) found that azimuth seismic anisotropy can induce large variations in the horizontal polarization of surface waves, which can be measured by the nine-component cross-correlation tensor (CCT) computed from ambient noise recorded by 3C sensors. Durand et al. (2011) observed a coseismic change of polarization directions, which varied strongly with station locations, measured from the 3C High Resolution Seismic Network (HRSN) associated with the Parkfield 2004 earthquake.

The present study is the part of seismic monitoring experiment conducted in the Changning-Weiyuan National Shale Gas Demonstration Zone inside the Sichuan basin in southwest China (Chen et al., 2018). Both short-period and broadband sensors were installed in borehole and surface with a variety of configurations to explore the most effective means in monitoring microearthquakes induced by hydraulic injections. Zuo et al. (2018) computed 3C cross correlograms of ambient noise data recorded by a 3C

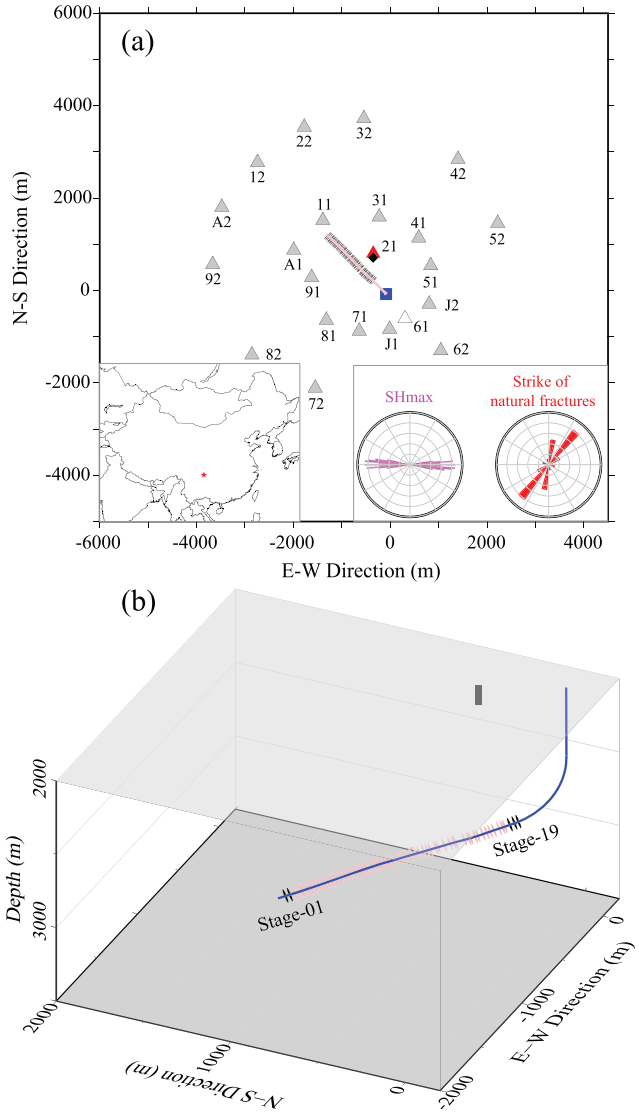

Figure 1. Map showing the experiment site. (a) Locations of the wellhead and horizontal well trajectory are indicated by the blue solid square and pink line, respectively. The black line segments indicate the position of water injection. Station 21, which is used for particle motion measurements, is indicated by red triangle. The black diamond indicates the shallow borehole array used in the study of Zuo et al. (2018). The blue square shows the wellhead and is also the location of a deep monitoring well, which was used to monitor the induced microseismicity by Meng et al. (2018). Station 61 has instrumental problem and is indicated by open triangle. The left bottom inset shows the location of the hydraulic fracturing experiment at the Weiyuan shale plate inside the Sichuan basin in southwest China (solid red star). The right bottom inset shows the orientations of the local maximum principal stress (magenta, left) and the strikes of the prevalent natural fractures (red, right), measured from well logging data, which are approximately N90°E and N40° to 60°E, respectively. (b) Three-dimensional view of the well trajectory. The blue line indicates the vertical (~3 km) and horizontal (~2 km) well trajectory. The pink and black line segments mark the position of water injection. For each stage, approximately 2,000 m^3 of water and 100 t of sands were injected. The thick black vertical bar indicates the horizontal location of the shallow borehole above the horizontal well.

vertical array installed in a shallow borehole (~300 m deep) at the site. They extracted clear *P* and *S* waves propagating vertically along the shallow borehole (surface to ~200 m) from the cross correlograms. They found that the shale play site has a strong azimuthal anisotropy depending on the polarization direction of the vertically propagating *S* waves, and the amplitude of seismic anisotropy dropped as much as 9% during a 19-stage hydraulic fracturing that lasted for 13 days. The measurement of Zuo et al. (2018) represents one particular point of the overburden above the hydraulic injection, while this study intends to extend this one-point measurement to the entire overburden above the horizontal well by using waveform data recorded by a 2-D surface broadband array.

In this study, we first used the continuous records of 21 broadband stations deployed over a circular area of ~5 km in diameter to compute surface wave Green's functions. We then employed a running window correlation-based coda wave interferometry technique (Snieder, 2006) to compute the temporal changes in seismic velocity across the array. The measured velocity changes showed a strong direction dependence, which was confirmed from the surface wave horizontal polarization data. Numerical modeling further suggested that the observed temporal variations were likely caused by stress changes induced by the hydraulic injection.

2. Data and Analyses

2.1. Seismic Monitoring of the Pilot Horizontal Drilling and Fracturing at Weiyuan

The seismic data of this study was from a comprehensive seismic monitoring experiment conducted in the Changning-Weiyuan National Shale Gas Demonstration Zone in the southwestern part of the Sichuan basin of China, which was selected by the Chinese government in 2012 to develop technology for shale gas exploition, such as horizontal drilling and hydraulic fracturing. Well logging and 3-D seismic surveys suggested that the Lower Cambrian Jiulaodong formation beneath the Weiyuan area is a marine shale layer at a depth of ~3,000 m with a thickness of ~300 m. It contains a set of organic-rich black shale rocks that serve as the primary source of shale gas reservoirs (Borkloe et al., 2016). A pilot horizontal well was drilled within the formation with a horizontal length of ~2,000 m along the NW-SE direction and a vertical depth of ~2,700 m (Figure 1). A 19-stage hydraulic fracturing stimulation was performed between 29 October and 10 November of 2014 except for 31 October. Details of the 19-stage injection treatment are listed in Table S1 in the supporting information. For each stage, roughly 2,000 m^3 of water and 100 t of sands were injected at a of ~2,600–2,700 m below the surface. We installed different types of seismic sensors with different configurations in order to better monitor the induced microseismicity, as well as subsurface structural changes associated with the hydraulic injections. In addition to the surface deployment, we also installed a string of 3C geophones in a deep monitoring well (Meng et al., 2018) and a shallow borehole (Zuo et al., 2018), which are shown by the blue square and black diamond in Figure 1a, respectively. In this study, we only used the surface broadband array to detect changes occurred inside the overburden of the horizontal injection well during the hydraulic injection.

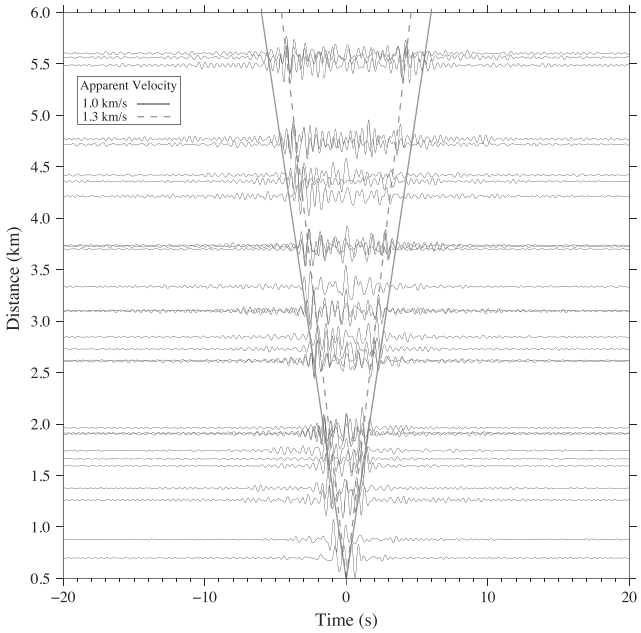

Figure 2. The reference NCFs used in calculating velocity changes between preinjection and coinjection are plotted in the order of station pair distance. The NCFs were filtered with a band-pass filter of 1–3 Hz.

As part of the surface deployment, we installed 22 broadband seismic stations around the wellhead with a station spacing ranging from a few hundred meters to a few kilometers to monitor the fracturing process over the entire range of treatment (Figure 1). Each station was equipped with a Guralp CMG-3T sensor and a Reftek 130 digitizer that was set to a sampling rate of 1,000 sample per second (sps). Since the system has a flat velocity response down to a period of 120 s, we anticipate that it can record a broad range of signals including microseisms with periods between a few seconds to a few tens of seconds. We started the broadband recordings on 22 October 2014, 6 days before the hydraulic injection to obtain a stable model of the ambient noise field before the treatment. The data were continuously recorded to 11 November 2014 with the same sampling rate. Among the 22 stations, Station 61 (Figure 1) was malfunctioning during a significant portion of the deployment, leading to a total of 21 stations in the final analyses.

2.2. Measuring Velocity Variations Using NCF-Based Coda Wave Interferometry

We used the vertical component records to compute daily noise cross-correlation functions (NCFs) for all the station pairs. The procedure we employed to preprocess the data was similar to that of Bensen et al. (2007). We cut the 1-day continuous seismic records into 10-min segments and then decimated them from 1,000 to 100 sps, as the ambient noise is distributed mainly in the frequency range of 0.5–6.0 Hz. Since all of the surface broadband stations were equipped with the same types of instruments, we did not deconvolve instrument response from the raw data, and directly employed the downsampled velocity records to compute the daily NCFs. We employed a running time window method with a window length of 60 s to compute NCFs using the 10-min records. If one of the records has a gap within the running window, the NCF of that time window is not computed. In order to obtain high-quality Green's functions from ambient noise data, it is important to minimize the influence of large deterministic arrivals of earthquakes in the continuous records (Wegler & Sens-Schönfelder, 2007). To do so, we applied spectral whitening to the seismograms. We first removed the linear trend and mean from the data for each time window and applied the Fourier transform to obtain the spectra of the two windows. We then reset the two amplitude spectra to 1.0 in the frequency range of 0.1–10.0 Hz and to 0.0 elsewhere while keeping the phase spectra unchanged. We further computed the cross-correlation function of the two windows by taking the inverse Fourier transform of the product of the modified spectrum of one window and the complex conjugate of the modified spectrum of the other one. We finally linearly stacked all the cross-correlation functions of the running windows to obtain the daily NCFs of each station pair. Since we had only partial recordings in the first and last days of the deployment, we found that the daily NCFs of these 2 days were of low quality due to insufficient stacking; therefore, we only used the 19 daily NCFs from 23 October to 10 November for each station pairs.

We band-pass filtered the NCFs in three frequency bands, 0.5–1.5, 1.0–3.0, and 2.0–6.0 Hz, and found that the intermediate band (1.0–3.0 Hz) yielded the highest signal-to-noise ratio (SNR) of the NCFs. We thus used the band-pass-filtered NCFs in 1.0–3.0 Hz for further analyses. In general, the daily NCFs show a clear Rayleigh wave arrival in both the causal and acausal windows (Figure 2). The coda waves after the Rayleigh wave in these NCFs, however, did not have sufficient SNR for making precise delay time measurements using the coda wave interferometry method described in the next section. Thus, we further computed the 3-day running average of the 19 daily NCFs to enhance the SNR of the coda waves. For example, we computed the average NFCs of 23–25 October as the 24 October daily NCF. The 23 October and 10 November daily NCFs were 2-day stacks of 23–24 October and 9–10 November, respectively.

The coda waves shown in Figure 2 are of high amplitude, suggesting that the uppermost crust at the experiment site is heterogeneous and the coda waves likely result from multiple scattering (Aki & Chouet, 1975). We also noticed that a few reference NCFs shown in Figure 2 have noticeable energy at time 0, which we attributed to insufficient stacking of ambient noise data or some unknown structures. The coda waves

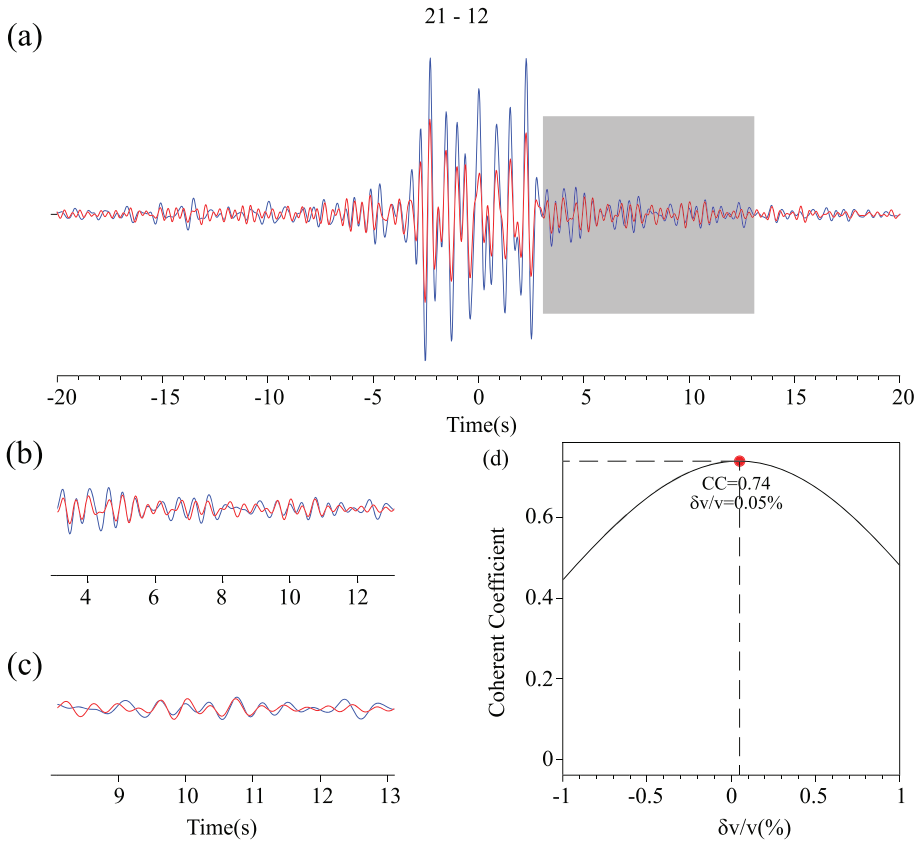

Figure 3. An example showing the application of coda wave interferometry to measure temporal variation between the reference and objective NCFs at the Station Pair 21-12. (a) The reference and objective NCFs are shown in blue and red lines, respectively. The gray shaded area indicates the first 10-s-long running window at the causal part. A total of eight running windows with a running step of 1 s at each side are used in interferometry measurement. (b) An amplified running window. (c) The second half window of (b). (d) The calculated cross-correlation coefficient (CC) is shown as a function of fractional velocity change, $\delta v/v$, which is used to compute the stretching/compressing factor (σ). The optimal $\delta v/v$ is obtained when the CC reaches the maximum.

travel longer in the crust than the Rayleigh wave and thus are expected to accumulate larger travel time anomalies due to multiple scattering in the crust. In particular, it has been shown that when there is a homogeneous change in the velocity field, the delay time (δt) increases linearly with the lapse time t (Niu et al., 2003; Snieder et al., 2002). The relative change of velocity, $\delta v/v$, is equal to the negative of the relative delay time, $-\delta t/t$. Hence, the relative change of velocity can be expressed as follows:

$$\delta t = -\frac{\delta v}{v} t \tag{1}$$

To estimate $\delta t/t$ associated with the hydraulic fracturing, we first stacked the six daily NCFs before the injection (from 23 to 28 October) to create a reference NCF for each station pair. We also stacked all the 13 daily NCFs between 29 October and 10 November, during which the 19-stage injection treatment was performed and referred them as coinjection NCFs. An example of the reference NCF and coinjection NCF of the Station Pair 21-12 is shown in Figure 3a. To further show the similarity of the coda field between the two NCFs, we enlarged the two segments of the coda windows in Figures 3b and 3c. We then computed cross-correlation coefficient between the reference NCFs and the 3-day or coinjection NCFs (referred as to objective NCFs) with a 10-s-long moving time window. We used a moving increment of 1 s and a total of eight running windows in both the causal and acausal parts of the NCFs. The start times of the coda windows were computed with an assumed apparent velocity of 1 km/s (solid line in Figure 2). For each moving window, we employed the stretching/compressing technique proposed by Sens-Schönfelder and Wegler (2006) to compute the $\delta t/t$

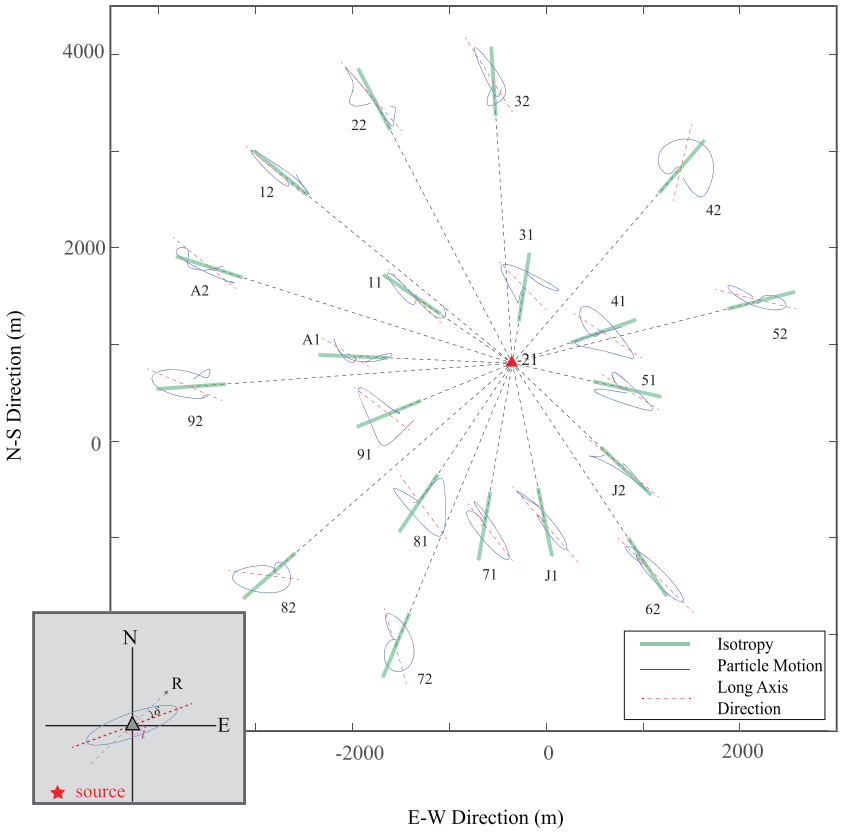

Figure 4. Surface wave horizontal particle motions measured from the NCFs computed with the vertical component of the virtual Source Station 21 and the two horizontal components of each station are shown in solid blue traces. The thick green segments indicate the direction of particle motions in isotropic media at each station, which are also the radial directions (thin black dashed lines). The red dashed lines only indicate the long axis direction of particle motion at each station. The gray schematic inset in the left-bottom corner shows the definition of the deviation angle δ. The back azimuth of the station is i. The red and black dashed lines show the long axis and radial directions, respectively.

between the reference and objective NCFs. This is done by stretching/compressing the time axis of the objective NCF by a scaling factor (σ) that is related to the fractional velocity change ($\delta v/v$):

$$\sigma = \frac{t + \delta t}{t} = 1 - \frac{\delta v}{v} \tag{2}$$

We grid searched the $\delta v/v$ in the range of −3% to 3% with an increment of 0.001% to find the optimum fractional velocity change ($\delta v/v$) that leads to the maximum cross-correlation coefficient (Figure 3d). We only chose measurements from windows with a CC ≥ 0.6 and selected pairs with more than four consistent measurements. We also applied the stretching method to the entire 18-s-long window to measure $\delta v/v$ *and* found that the results are generally in good agreement with the subwindowing measurements. One advantage using multiple windows in measuring velocity perturbations is that we can compare results from different windows to select robust measurements of $\delta v/v$.

2.3. Estimating Changes in Ballistic Surface Wave Horizontal Polarization Direction

Additionally, we investigated changes in seismic anisotropy associated with the hydraulic injection by examining temporal variations in the horizontal polarization direction of ballistic surface waves. We followed the method of Lin et al. (2014) to compute the horizontal motion of the surface waves from ambient noise data. The data preprocessing method was the same as described in section 2.2. After the daily NCFs were computed, we further calculated the 3-day moving averages of the daily NCFs. Since the 3-day average was not

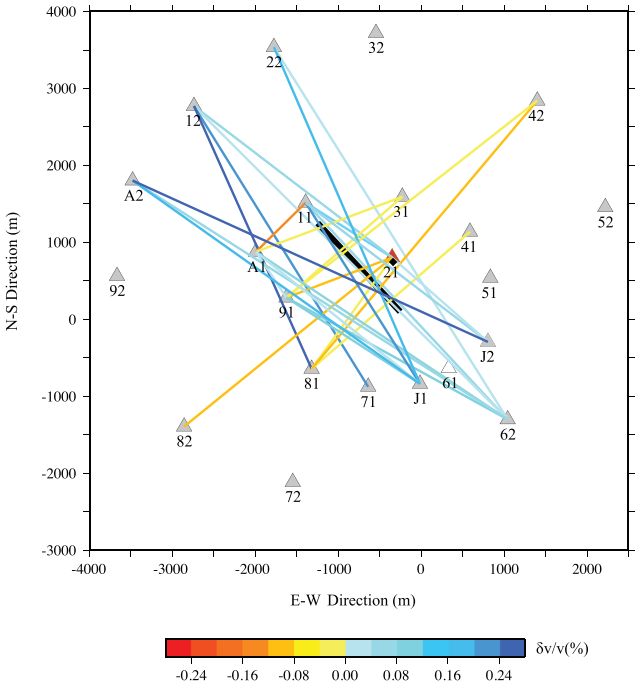

Figure 5. Map showing the results of the coda wave interferometry measurements. Fractional velocity changes ($\delta v/v$) measured between the preinjection and coinjection periods along different paths are shown in color, with "cold" and "warm" colors indicating velocity increase and decrease, respectively. The black line denotes the horizontal well trajectory. Triangles indicate the broadband stations.

available for the first (23 October) and the last (10 November) daily NCFs, in this part of the study, we analyzed the seventeen 3-day-averaged NCFs from 24 October to 9 November. To examine whether the horizontal propagation direction of the ambient-noise-derived surface waves varies with azimuth, we selected station 21 (red solid triangle in Figure 1a) as the virtual source, and the rest of stations as receivers (except for station 61). We computed the two NCFs, Z-N and Z-E for all the receivers. Here the first and second letters refer to the component of the virtual source and receiver stations, respectively, while Z, N, and E represent the vertical, north-south, and east-west components, respectively.

We band-pass filtered the NCFs in the frequency band of 0.1–1.0 Hz, which seems to have the best SNR for the ballistic surface waves since this frequency band covers the secondary microseism peak. We found the best frequency band here is different from that (1.0–3.0 Hz) of the Z-Z NCFs that we analyzed in the previous section. Such a difference might be related to the fact that we are using the ballistic surface wave here while the previous section uses the coda wave field, which generally has higher frequency contents than the main surface wave signal. The ballistic surface waves in the frequency band of 0.1–1.0 Hz travel mostly in the top ~4 km of the crust, so they are expected to have some sensitivity of the horizontal treatment well, which is located at ~3.0 km below the surface.

The horizontal particle motions of the surface waves at 20 stations are shown in Figure 4 (blue solid line). To estimate the horizontal polarization direction of the surface wave, we first calculated the covariance matrix from the Z-N and Z-E NCFs (Niu & Li, 2011):

$$c_{ij} = \int_{T1}^{T2} u_i(t) u_j(t) dt \qquad i, j = 1, 2 \tag{3}$$

Here T_1 and T_2 define the time window of the ballistic surface wave signal. We employed an apparent velocity of 1.3 km/s (Figure 2) to estimate the peak arrival time T_0, and set $T_{2,1} = T_0 \pm 1.0$ s. u_i and u_j are the Z-E and Z-N NCFs, respectively. In the absence of noise and in an isotropic medium, the covariance matrix c, is expected to possess one nonzero eigenvalue, and the direction of the corresponding eigenvector is expected to be parallel to the back azimuthal direction. When the medium is azimuthally anisotropic, and/or when noise is present, the covariance matrix $\boldsymbol{c}$, is expected to have two nonzero eigenvalues, λ_1 and λ_2, where $|\lambda_1| \geq |\lambda_2|$. The ratio of the absolute values of the two eigenvalues, $|\lambda_2|/|\lambda_1|$, defines the linearity of the particle motion, and the polarization direction is parallel to the eigenvector of the first eigenvalue. We define a deviation angle, δ, to be the difference between the radial direction and polarization direction (Figure 4 inset), which is measured clockwise from the radial direction and varies from −90° and 90°. In an azimuthal anisotropic medium, we expect δ to change periodically with the radial direction, or the back azimuth with a period of 180°, and to be minimum along the symmetry axis of the anisotropic medium, that is, either the fast or the slow direction.

In order to determine how δ varies with radial direction, we employed a harmonic analysis of the measured deviation angles as a function of the horizontal incident angle (i), which is defined as the opposite direction of the back azimuthal direction (inset in Figure 4):

$$\delta(i) = \sum_{n=0}^{9} A_n \cos\{n(i - \varnothing_n)\} \tag{4}$$

Here n is the harmonic degree, which was varied from 0 to 9, A_n is the deviation angle amplitude, and ϕ_n is the initial angle of the n^{th} degree harmonic function. Since the medium in our study area features a strong azimuthal anisotropy (Zuo et al., 2018), we expect the dominant harmonic degree to be $n = 2$.

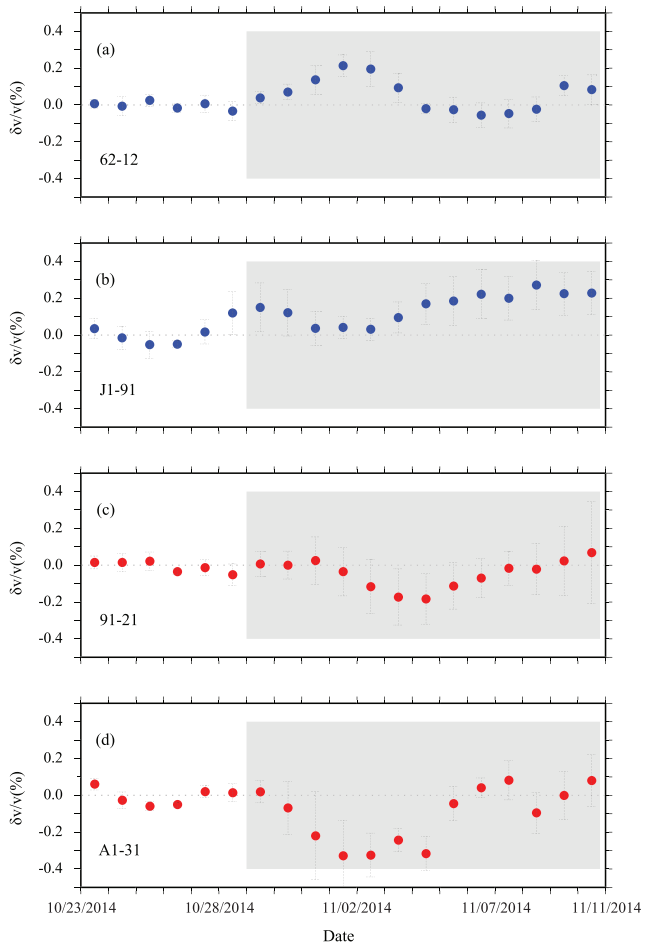

Figure 6. Temporal velocity changes measured between the 3-day-averaged NCFs and the reference NCF. Panels (a) and (b) are the results of two station pairs with their path direction approximately parallel to the horizontal well trajectory. Panels (c) and (d) are similar to (a) and (b) except for the path direction, which is approximately perpendicular to the horizontal well. The gray shaded areas denote the hydraulic injection period.

3. Results

3.1. Direction-Dependent Relative Velocity Changes

To investigate overall changes induced by the hydraulic fracturing stimulation, we applied the coda wave interferometry analyses described in section 2.2 to the coinjection NCFs of all the station pairs of the 21 stations. For each pair, we obtained the fractional velocity changes ($\delta v/v$) and the cross-correlation coefficients (*CCs*) from a total of sixteen 10-s moving windows, eight from the causal part and another eight from the acausal part of the coda field. For many time windows in the later part of the coda, the *CCs* are very small due to the low SNR, resulting in unstable measurements of $\delta v/v$. We found that *CCs* of the first two windows of causal and acausal parts usually had the largest values among the 16 measurements. It has been shown that errors in cross-correlation-based time measurements depend on the SNR of the coda waves (Cheng et al., 2007; Niu et al., 2003). To accurately estimate $\delta v/v$ from coda waves with a dominant frequency range of 1–3 Hz, we expect the coda waves to have an SNR greater than 5, and a corresponding CC of greater than 0.6. We thus only selected windows with $CCs \geq 0.6$, and station pairs with more than four selected windows. We further computed the average ($[\delta v/v]_{ave}$) and standard deviation ($[\delta v/v]_{dev}$) of the fractional velocity changes from the multiple windows and selected the ones with the absolute value of $[\delta v/v]_{ave}$ to be greater than $[\delta v/v]_{dev}$.

The hydraulic fracturing induced seismicity appeared to spread across an elongated area of ~2 km along the horizontal well direction with a width of ~1 km (Chen et al., 2018; Meng et al., 2018). We thus restricted stations pairs that sample the SRV. We computed the distance from the midpoint of the two stations to the midpoint of the well trajectory and selected the pairs with the distance less than 1.5 km. Zuo et al. (2018) found direction-dependent changes in the *S* wave velocity associated with the hydraulic treatment with an average velocity variation of 9% along the direction of the horizontal well trajectory. They employed a simple crack opening model at 3 km depth and found that large strain/stress changes in the directions either parallel or perpendicular to the NW-SE oriented horizontal well trajectory. We thus focused on ray paths that are along these two directions, which are expected to have large accumulative traveltime changes. More specifically, we only selected the station pairs with an azimuth between 30° and 70° or between 120° and 160°. Measurements of $\delta v/v$ from station pairs along the other directions were less consistent than those of the above two directions. The positive and negative mixed velocity changes obtained from two azimuthal ranges (30–70° and 120–160) suggested a complicated scenario in structural changes associated with the injection, which were likely distributed heterogeneously and anisotropically in space.

After following the above processing, we were able to obtain robust $\delta v/v$ measurements from 28 pairs, which are shown in Figure 5 and further listed in Table S2. We found that all paths of station pairs in the NW-SE direction (i.e., roughly parallel to the horizontal well trajectory) showed increases in propagation velocity (blue lines in Figure 5) ranging from 0.01% to 0.39%. On the other hand, paths in the NE-SW direction (i.e., roughly perpendicular to the well trajectory) experienced wave speed reduction in the range of −0.15% to −0.03%. On the other hand, results from other paths are highly scattered and mixed with positive and negative changes (Figure S1).

Figure 5 illustrates clear direction-dependent wave speed changes between the 6-day preinjection period and the 13-day coinjection period. In order to examine when these changes occurred, we selected four station pairs, two from each of the two directions. For each pair, we used the stacked NCFs of the 6-day preinjection period as the reference, and cross correlated it with the 3-day-averaged 19 daily NCFs. The measured

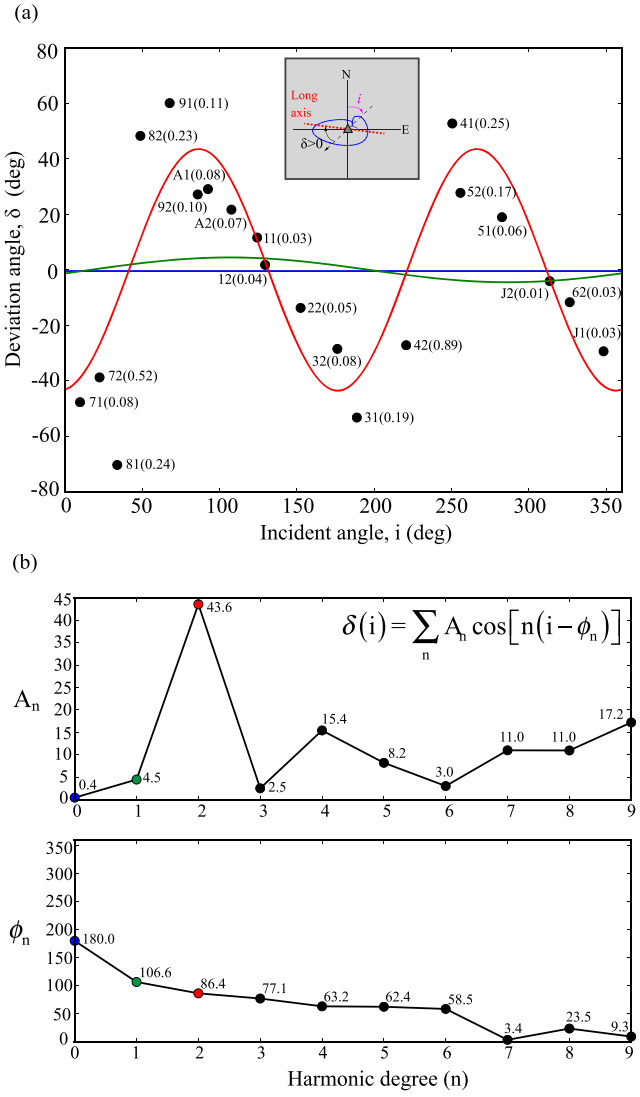

Figure 7. (a) The deviation angle δ measured from the horizontal NCFs on 10/24/2014 (solid black circles) is shown as a function of station back azimuth. The numbers inside the parenthesis after the station name indicating the linearity of particle motion, which is the ratio of the absolute values of the difference between two eigenvalues, $|\lambda_2|/|\lambda_1|$ (see main text for more details). The ratio varies from 0 to 1. A number close to 0 means the particle motion is close to linear while a number close to 1 means that the particle motion is close to a circle. The blue, green and red lines correspond to the zeroth-, first-, and second-degree harmonic variations, respectively. The gray schematic defines the deviation angle δ and the back azimuthal incident angle i. (b) Results of the harmonic analysis of the data shown (a). The top and bottom figures show the deviation amplitude and initial angle at harmonic degree from 0 to 9.

fractional velocity changes ($\delta v/v$) at the two NW-SE oriented pairs 62-12 and J1-91 and the two NE-SW direction pairs 91-21 and A1-31 are shown in Figures 6a and 6b, and Figures 6c and 6d, respectively. Measurements of the other 24 pairs are shown in Figure S2. In the preinjection period, the measured fractional velocity changes are relatively small, suggesting that the 3-day smoothed changes in wave speed are insignificant before the fluid injection. Once the hydraulic fracturing started on 29 October 2014, the changes of velocity along the 62-12 path began to rise, peaked at on 1 November 2014, and became insignificant in the second half of the injection period (Figure 6a). For the J1-91 path, the velocity increase in the first half of the injection period was rather small but became significant toward the end of the injection (Figure 6b). For the two perpendicular paths of 91-21 and A1-31, we found significant velocity reductions in the middle of fluid injection (Figures 6c and 6d). The small fluctuations observed before the injection period are likely related the reference NCFs that we used here, which was stacked from data recorded before the injection. If the coinjection period NCFs were selected as the reference, the preinjection fluctuations could have been more significant. Both cases would suggest, however, that there was a significant change between the two periods.

3.2. Temporal Variation in Ballistic Surface Wave Polarization Direction and Seismic Anisotropy

The deviation angles of the ballistic surface wave polarization direction calculated with the covariance matrix method described in section 2.3 are shown in Figure 7a. Here, we plotted the measured deviation angle, δ, as a function of incident angle, i, which showed a clear periodic variation (Figure 7a). We further employed the harmonic analysis to compute the deviation angle amplitudes and initial angles of each harmonic degree, which were shown in Figure 7b. It is clear that the deviation angle amplitude reached its maximum at the harmonic degree of 2 (Figure 7b). The corresponding deviation angle amplitude A_2 and initial phase ϕ_2 were 43.6° and 86.4°, respectively. Their predicted azimuthal variation is shown in Figure 7a (red solid line). Based on ϕ_2, we further obtained the orientation of the anisotropic symmetry axis, ϕ_a, to be 131.4°, since $\cos 2(\phi_a - \phi_2) = 0$, $\phi_a = \pi/4 + \phi_2$.

We applied the harmonic analysis to all the seventeen 3-day moving averages of the daily NCFs. All of the NCFs showed a harmonic degree of 2, and the measured 17 pairs of (A_2, ϕ_2) are shown in Figures 8a and 8b, respectively. The maximum deviation angle A_2 stayed roughly the same in the preinjection period and started to drop right after the injection (vertical dashed line in Figure 8a). The reduction of A_2 peaked at 2 November 2014 and remained at a slightly decreased value for approximately 1 week before diminishing to almost zero at the end of the injection (Figure 8a). The maximum reduction was ~33% (i.e., from ~45° to ~30°). The ϕ_2 remained roughly the same throughout the entire treatment (Figure 8b).

4. Discussion

The harmonic analysis of surface wave polarization directions indicated a clear harmonic degree-2 azimuthal variation of the measured deviation angles (Figure 7), suggesting the presence of azimuthal anisotropy in the study area. Tanimoto (2004) showed that the deviation angle reaches its minimum in fast or slow direction, which means that the fast or slow direction is $\pm\pi/4 + \phi_2$, that is, N131.4°E or N41.4°E.

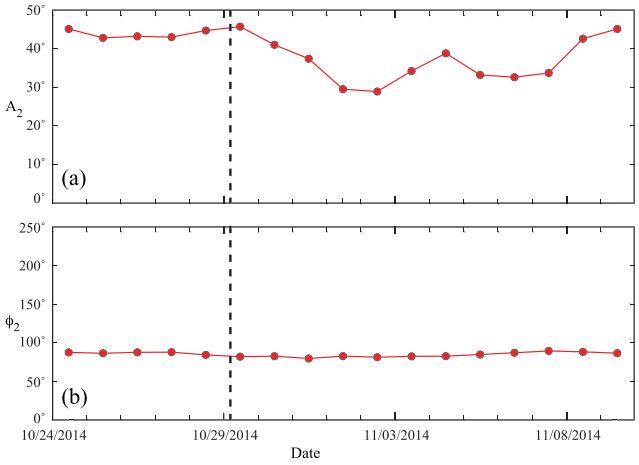

Figure 8. Temporal variations of amplitude and initial angle of the degree-2 harmonics are shown in the top (a) and bottom (b), respectively. The vertical dashed lines mark the beginning of hydraulic fracturing.

The latter aligns well with the direction of preexisting fractures (Chen et al., 2018). Zuo et al. (2018) computed cross-correlation functions of ambient noise recorded by a vertical array installed in a shallow borehole in the treatment site (black solid diamond in Figure 1a) and found the top ~200 m of the medium possesses a strong azimuthal anisotropy. The fast polarization direction is ~N45°E, and changes to ~N65°E during the treatment (Table 1 in Zuo et al., 2018). Therefore, our measurement of N41.4°E is in good agreement with the body wave data of the pretreatment level. Since the measurement of Zuo et al. (2018) represents changes around the 200-m deep shallow borehole, while our estimate is the average of the circular area with a diameter of ~5 km covered by the array (Figure 4), we think the slight difference between the two measurements is reasonable. Unlike the body wave data, our measurements of the fast direction angle did not show significant changes during the treatment (Figure 8b), and we speculated that since borehole is located just above the horizontal well, it is likely that the injection had more influence on the shallow borehole site than the average of the circular area covered by the broadband array. On the other hand, the amplitude of the deviation angle, A_2, did show a significant reduction as the treatment started on 29 October (Figure 8a), which is consistent with the body wave observation (Zuo et al., 2018).

In general, the surface wave horizontal polarization direction data agree well with the shallow borehole body wave results in terms of seismic anisotropy. The Weiyuan shale play site has a strong azimuthal seismic anisotropy and the amplitude of seismic anisotropy started decrease once the hydraulic treatment began. The scenario of injection induced weakening of seismic anisotropy is also consistent with the observed direction-dependent velocity changes from the Rayleigh wave coda data. The measured seismic velocity changes between preinjection and coinjection (Figure 5) showed a clear increase along raypaths in the NW-SE direction, and a slight decrease in the NE-SW direction. Here we argue that the observed velocity changes between the two periods are likely to be induced by the hydraulic injection, since daily variations measured at the station pairs clearly showed that significant velocity changes occurred only after the injection (Figure 6). The velocity increase in the slow direction (NW-SE), together with a velocity reduction in the fast direction (NE-SW) shown by the coda wave data suggested a weakening of azimuthal anisotropy, which was also indicated by the surface polarization data shown in Figure 8a and the shallow well results of Zuo et al. (2018). However, velocity changes measured from the Rayleigh wave coda is ~0.12% and ~ −0.06% on average along the slow and fast directions, respectively, much smaller than the ~9% increase in the slow direction by the shallow well data (Zuo et al., 2018). As mentioned above, the measurements from the surface wave coda wave interferometry represented average velocity changes across the array while the vertically propagating *S* wave along the shallow borehole reflected changes at one site very close to the injection located at the array center. Thus, we argue that the injection-induced velocity changes are likely very heterogeneous in space and centered at the treatment. On the other hand, we also observed a large amplitude reduction of ~15.8% (from ~43.82° to ~36.88°) in the deviation angle, A_2, related to the hydraulic fracturing, which might suggest that the horizontal polarization direction is very sensitive to azimuthal anisotropy (Saade et al., 2015). We found that it is very difficult to find a model that can quantitatively explain both the coda wave and polarization data and would like to investigate the issue in a separate 3-D numerical study.

The Weiyuan shale play site is experiencing a large horizontal differential stress up to 24.7 MPa largely due to the India-Eurasia collision. Well logging and core sample analysis (Liang et al., 2015) indicated that a large amount of preexisting natural fractures at various scales were aligned predominantly in the directions of N40° to 60°E, oblique to the orientation of the maximum horizontal compressional stress (MHCS), which is roughly in the EW direction (Figure 1a). It is generally believed that seismic anisotropy observed in the upper crust is caused by alignment of the preexisting fractures/cracks with rocks, which is related to the current stress field (Boness & Zoback, 2004; Crampin & Chastin, 2003; Crampin & Lovell, 1991) since the stress field can preferentially open/close cracks in certain directions. If the initial preexisting fractures/cracks are randomly oriented, then fractures/cracks perpendicular to the MHCS direction tend to be closed, leading

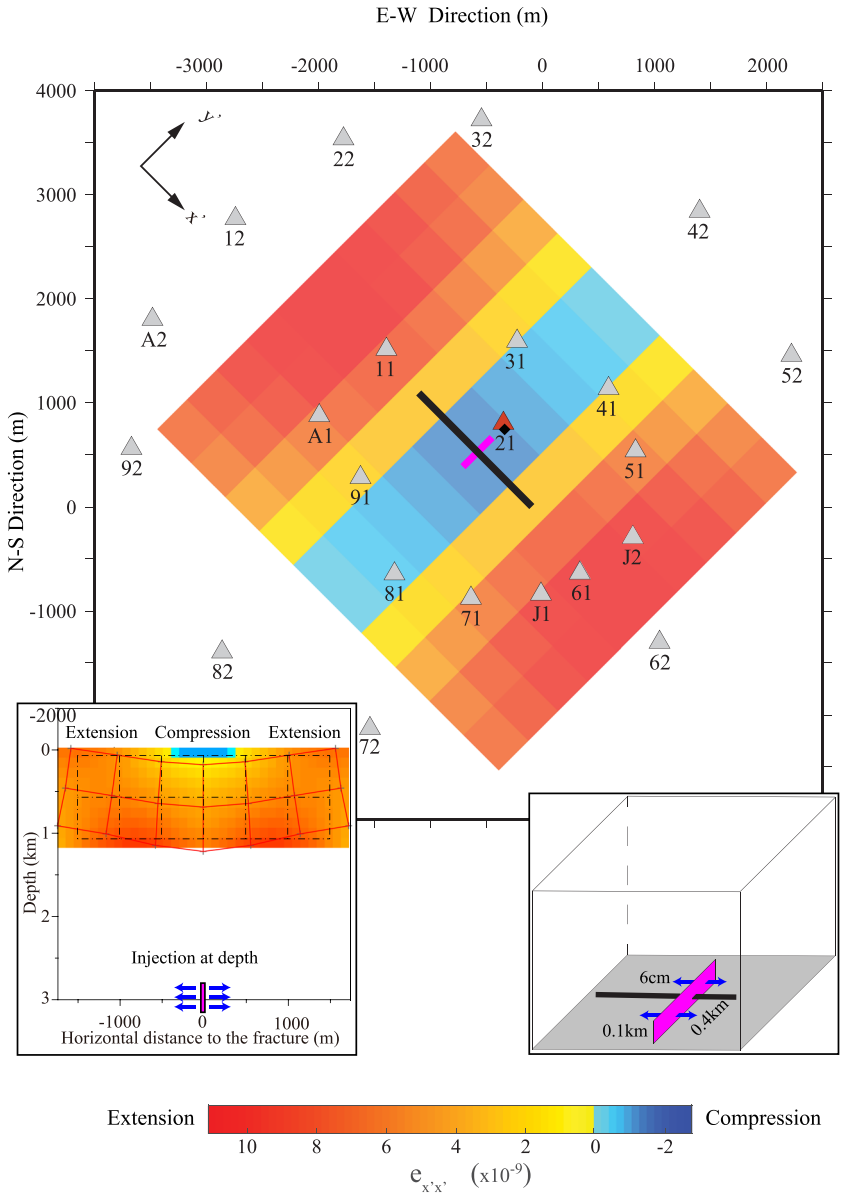

Figure 9. Map showing strain $e_{x'x'}$ calculated at surface with x' indicating the NW-SE direction. The amplitude of the strain is shown in color with "cold" and "warm" colors representing areas under horizontally compression and extension along the x' axis, respectively. The thick black line indicates the horizontal well, and the purple solid line segment represents the tensile fault located at 3 km deep. Here the fault is placed in the middle of the horizontal well. Triangles indicate the locations of the broadband stations. Inset at the left bottom show the normal strain of the top 1 km of a depth section along the horizontal well direction (NW-SE). The red solid meshes are the deformed black dashed meshes and are exaggerated by a factor of 4×10^8. The vertical purple rectangle indicates the injection-induced tensile fracture. Inset at the right bottom is a 3-D view of the schematic tensile fracture with length of 0.4 km, width of 0.1 km and dislocation of 6 cm located at 3 km depth.

to a preferred orientation of fractures/cracks parallel to the MHCS direction, which is also the fast polarization direction for a nearly vertically propagating S wave. Thus, the observed seismic velocity changes here are likely to be caused by the opening or closure of cracks in response to stress changes induced by fluid injection.

In order to make a rough estimate of the stress changes within the overburden of the horizontal well induced by the fluid injection at ~3 km, we employed the uniform half-space method of Okada (1992) to compute the strain field caused by a deep tensile fault. We set up a vertical rectangular fault centered at 3 km deep with a

strike perpendicular to the horizontal well trajectory. Based on the lateral and vertical extension of the recorded microseismicity (Meng et al., 2018), we set the vertically dipping fault to be 400 m long and 100 m wide in the horizontal and vertical directions (right-bottom inset of Figure 9), respectively. The hydraulic injection treatment was divided into 19 stages, and for each stage roughly 2,000 m^3 of water and 100 t of sands (Chen et al., 2018) were injected. We further set a tensile dislocation of 0.06 m by assuming the fault space is roughly similar to the injection volume of one stage.

The computed tensile strain along the horizontal well direction at the surface is shown in the Figure 9. Most surface areas are under extension along the NW-SE direction except for the middle part, an NE-SW elongated band with a width of ~800 m right above the tensile fault, which is compressed in the NW-SE direction. The areal strain also showed a similar pattern. It should be noticed here that the model shown here represented hydraulic fracturing for one stage with a highly simplified tensile fault. The actual faulting occurred during the 19-stage fracturing should be more complicated, but we would expect that the lateral variation and the amplitude order of the strain are somewhat intuitive. The maximum cumulative extensional and compressional strain is in the order of 10^{-7}, which is converted to 3×10^3 Pa with an assumed bulk modulus of 30 GPa.

Chen et al. (2018) found that the injection-induced seismicity formed two recognizable lineaments with a NE-SW trending, which is consistent with the predominant direction of the preexisting faults and fractures (Liang et al., 2015). Zuo et al. (2018) found that the shale play site has a distinct azimuthal seismic anisotropy with a fast polarization direction of ~N45°E, which is also in good agreement with the alignment of the NE-SW oriented natural fracture system. Thus, we expect that an increase of compressional stress in the NW-SE direction can cause closure of natural fractures, leading to the observed increase of *S* wave velocity in the NW-SE direction. On the other hand, the increase of normal stress in the NW-SE direction might have led to the opening of small amount of vertical fractures in its perpendicular direction (NE-SW) due to fluid migration, which could cause the observed increase of seismic velocity in the NE-SW direction.

As mentioned in section 1, laboratory studies indicated that seismic velocities of crustal rocks change slightly with the stress level they are subjected to (e.g., Birch, 1960; Nur & Simmons, 1969; Scholz, 1968). The velocity-stress sensitivity was measured to be approximately 10^{-7} Pa^{-1} at Earth's surface and around 10^{-9} Pa^{-1} at ~1 km depth (e.g., Birch, 1960; Nur & Simmons, 1969). The velocity-stress sensitivity estimated from field studies (Niu et al., 2008; Silver et al., 2007; Yamamura et al., 2003; Yang et al., 2018) is slightly broader, in the range of 10^{-6} to 10^{-9} Pa^{-1}. Using the observed average velocity change of ~0.12% and the calculated maximum stress increase of 3×10^3 Pa, we obtain a velocity-stress sensitivity of 4×10^{-7} Pa^{-1}, which falls in the middle of the observed values. Since we used the maximum stress and average velocity change in computing the velocity-stress sensitivity here; therefore, the estimate here could be considered as the low end-member and the actual sensitivity is likely higher. Also, the coda waves consist of scattered surface and body waves, which have better depth sensitivity than pure surface waves; therefore, the observed stress sensitivity represents an average over a certain depth range, which is expected to be smaller than those measurements at Earth's surface.

5. Conclusions

We computed the noise cross-correlation functions using continuous data recorded by a small-scale broadband array deployed to monitor a hydraulic fracturing treatment at the Weiyuan shale play site inside the Sichuan basin in southwest China. To investigate subsurface structural changes induced by the hydraulic injection, we first applied coda wave interferometry method to the vertical component to estimate temporal velocity changes across the array. We then computed the covariance matrix of the main surface wave recorded on the two horizontal components to estimate the temporal variations of horizontal polarization direction. The measured velocity changes associated with the hydraulic injection showed an increase of ~0.12% in the NW-SE direction and a slightly decrease of −0.06% in the NE-SW direction, respectively. The measured surface wave polarization directions showed a periodic deviation in the azimuthal direction, indicating the presence of azimuthal seismic anisotropy at the injection site. The amplitude of deviation decreased significantly during the injection period, suggesting a weakening of seismic anisotropy. Both observations indicate direction-dependent changes in seismic velocity during the treatment, which can be explained by closure of preexisting vertical faults and fractures with strikes in the NE-SW direction. Simple numerical modeling suggested that injection at 3 km deep could introduce a compressional stress

field along NW-SE direction at the surface right above the injection. The induced stress change can reach to tens of kilopascals, resulting in velocity changes of a few tenths of percent with a reasonable velocity-stress sensitivity of 10^{-7} Pa^{-1}.

Data Availability Statement

The NCF data are available at https://doi.org/10.17632/dnd3n74n43.1 website, and the final derived data reported in this paper are included in the supporting information.

Acknowledgments

We would like to thank Sichuan Geophysical Company of China National Petroleum Company (CNPC) (http://ccde.cnpc.com.cn/) for providing the field data set and permission to publish this work. We also thank the Editor, Associate Editor, and the three anonymous reviewers for their constructive and thoughtful comments and suggestions, which have significantly improved the quality of this paper. This study was jointly supported by the Project of China Seismic Experimental Site (2019CSES35), National Key R&D Program of China (2017YFC1500303), and the National Natural Science Foundation of China (Grant 41630209).

References

Aki, K., & Chouet, B. (1975). Origin of coda waves: Source, attenuation, and scattering effects. *Journal of Geophysical Research*, *80*(23), 3322–3342. https://doi.org/10.1029/JB080i023p03322

Angerer, E., Crampin, S., & Li, X. Y. (2000). In *Changes in shear wave anisotropy in time-lapse data: A case study*. Glasgow, Scotland: 62nd EAGE Conference & Exhibition. https://doi.org/10.3997/2214-4609-pdb.28.X38

Bensen, G. D., Ritzwoller, M. H., Barmin, M. P., Levshin, A. L., Lin, F., Moschetti, M. P., et al. (2007). Processing seismic ambient noise data to obtain reliable broad-band surface wave dispersion measurements. *Geophysical Journal International*, *169*(3), 1239–1260. https://doi.org/10.1111/j.1365-246X.2007.03374.x

Birch, F. (1960). The velocity of compressional waves in rocks to 10 kilobars, Part 1. *Journal of Geophysical Research*, *65*(4), 1083–1102. http://doi.org/10.1029/JZ065i004p01083

Boness, N. L., & Zoback, M. D. (2004). Stress-induced seismic velocity anisotropy and physical properties in the SAFOD Pilot Hole in Parkfield, CA. *Geophysical Research Letters*, *31*, L15S17. https://doi.org/10.1029/2003GL019020

Borkloe, J. K., Pan, R. F., Jin, J. N., Nyantakyi, E. K., & Meng, J. H. (2016). Evaluation of shale gas potential of Cambrian Jiulaodong formation in Wei-201 well block in Sichuan Basin, China. *Interpretation*, *4*(2), T123–T140. https://doi.org/10.1190/INT-2015-0074.1

Brenguier, F., Campillo, M., Takeda, T., Aoki, Y., Shapiro, N. M., Briand, X., et al. (2014). Mapping pressurized volcanic fluids from induced crustal seismic velocity drops. *Science*, *345*(6192), 80–82. https://doi.org/10.1126/science.1254073

Brenguier, F., Shapiro, N. M., Campillo, M., Ferrazzini, V., Duputel, Z., Coutant, O., & Nercessian, A. (2008). Towards forecasting volcanic eruptions using seismic noise. *Nature Geoscience*, *1*(2), 126–130. https://doi.org/10.1038/ngeo104

Byerley, G., Monk, D., Aaron, P., & Yates, M. (2018). Time-lapse seismic monitoring of individual hydraulic frac stages using a downhole DAS array. *The Leading Edge*, *37*(11), 802–810. https://doi.org/10.1190/tle37110802.1

Chen, H., Ge, H., & Niu, F. (2014). Semiannual velocity variations around the 2008 M w 7.9 Wenchuan earthquake fault zone revealed by ambient noise and ACROSS active source data. *Earthquake Science*, *27*(5), 529–540. https://doi.org/10.1007/s11589-014-0089-5

Chen, H., Meng, X., Niu, F., Tang, Y., Yin, C., & Wu, F. (2018). Microseismic monitoring of stimulating shale gas reservoir in SW China: 2. Spatial clustering controlled by the preexisting faults and fractures. *Journal of Geophysical Research: Solid Earth*, *123*, 1659–1672. https://doi.org/10.1002/2017JB014491

Cheng, X., Niu, F., Silver, P. G., Horiuchi, S., Takai, K., Iio, Y., & Ito, H. (2007). Similar microearthquakes observed in western Nagano, Japan, and implications for rupture mechanics. *Journal of Geophysical Research*, *112*, B04306. https://doi.org/10.1029/2006JB004416

Cheng, X., Niu, F., & Wang, B. (2010). Coseismic velocity change in the rupture zone of the 2008 Mw 7.9 Wenchuan earthquake observed from ambient seismic noise. *Bulletin of the Seismological Society of America*, *100*(5B), 2539–2550. https://doi.org/10.1785/0120090329

Corciulo, M., Roux, P., Campillo, M., & Dubucq, D. (2012). Instantaneous phase variation for seismic velocity monitoring from ambient noise at the exploration scale. *Geophysics*, *77*(4), Q37–Q44. https://doi.org/10.1190/geo2011-0363.1

Corciulo, M., Roux, P., Campillo, M., Dubucq, D., & Kuperman, W. A. (2012). Multiscale matched-field processing for noise-source localization in exploration geophysics. *Geophysics*, *77*(5), KS33–KS41. https://doi.org/10.1190/geo2011-0438.1

Crampin, S., & Chastin, S. (2003). A review of shear wave splitting in the crack-critical crust. *Geophysical Journal International*, *155*(1), 221–240. https://doi.org/10.1046/j.1365-246X.2003.02037.x

Crampin, S., & Lovell, J. H. (1991). A decade of shear-wave splitting in the Earth's crust: What does it mean? What use can we make of it? And what should we do next? *Geophysical Journal International*, *107*(3), 387–407. https://doi.org/10.1111/j.1365-246X.1991.tb01401.x

De Ridder, S. A. L., & Biondi, B. L. (2013). Daily reservoir-scale subsurface monitoring using ambient seismic noise. *Geophysical Research Letters*, *40*, 2969–2974. https://doi.org/10.1002/grl.50594

Delatre, M., & Manceau, J. C. (2013). Applicability of long-range seismic noise correlation for CO_2 geological storage monitoring. *Energy Procedia*, *37*, 4049–4056. https://doi.org/10.1016/j.egypro.2013.06.305

Durand, S., Montagner, J. P., Roux, P., Brenguier, F., Nadeau, R. M., & Ricard, Y. (2011). Passive monitoring of anisotropy change associated with the Parkfield 2004 earthquake. *Geophysical Research Letters*, *38*, L13303. https://doi.org/10.1029/2011GL047875

Froment, B., Campillo, M., Chen, J. H., & Liu, Q. Y. (2013). Deformation at depth associated with the 12 May 2008 Mw 7.9 Wenchuan earthquake from seismic ambient noise monitoring. *Geophysical Research Letters*, *40*, 78–82. https://doi.org/10.1029/2012GL053995

Guilbot, J., & Smith, B. (2002). 4-D constrained depth conversion for reservoir compaction estimation: Application to Ekofisk Field. *The Leading Edge*, *21*(3), 302–308. https://doi.org/10.1190/1.1463782

Herwanger, J. V., & Horne, S. A. (2009). Linking reservoir geomechanics and time-lapse seismics: Predicting anisotropic velocity changes and seismic attributes. *Geophysics*, *74*(4), W13–W33. https://doi.org/10.1190/1.3122407

Hillers, G., Ben-Zion, Y., Campillo, M., & Zigone, D. (2015). Seasonal variations of seismic velocities in the San Jacinto fault area observed with ambient seismic noise. *Geophysical Journal International*, *202*(2), 920–932. https://doi.org/10.1093/gji/ggv151

Hillers, G., Husen, S., Obermann, A., Planes, T., Larose, E., & Campillo, M. (2015). Noise-based monitoring and imaging of aseismic transient deformation induced by the 2006 Basel reservoir stimulation. *Geophysics*, *80*(4), KS51–KS68. https://doi.org/10.1190/geo2014-0455.1

Hillers, G. T., Vuorinen, T. A., Uski, M. R., Kortstrom, J. T., Mantyniemi, P. B., Tiira, T., et al. (2020). The 2018 geothermal reservoir stimulation in Espoo/Helsinki, southern Finland: Seismic network anatomy and data features. *Seismological Research Letters*, *91*(2A), 770–786. https://doi.org/10.1785/0220190253

Lecocq, T., Longuevergne, L., Pedersen, H. A., Brenguier, F., & Stammler, K. (2017). Monitoring ground water storage at mesoscale using seismic noise: 30 years of continuous observation and thermo-elastic and hydrological modeling. *Scientific Reports*, *7*(1), 14241. https://doi.org/10.1038/s41598-017-14468-9

Liang, X., Liu, X., Shu, H., Xian, C. G., Zhang, Z., Zhao, C. D., & Zhang, L. (2015). *Characterization of complex multiscale natural fracture systems of the Silurian LongMaXi Gas Shale in the Sichuan Basin, China*. SPE Asia Pacific Unconventional Resources Conference and Exhibition, Society of Petroleum Engineers. https://doi.org/10.2118/176938-MS

Lin, F. C., Tsai, V. C., & Schmandt, B. (2014). 3-D crustal structure of the western United States: Application of Rayleigh-wave ellipticity extracted from noise cross-correlations. *Geophysical Journal International*, *198*(2), 656–670. https://doi.org/10.1093/gji/ggu160

Lobkis, O. I., & Weaver, R. L. (2001). On the emergence of the Green's function in the correlations of a diffuse field. *The Journal of the Acoustical Society of America*, *110*(6), 3011–3017. https://doi.org/10.1121/1.1417528

Maxwell, S. C., Rutledge, J., Jones, R., & Fehler, M. (2010). Petroleum reservoir characterization using downhole microseismic monitoring. *Geophysics*, *75*(5), 75A129–75A137. https://doi.org/10.1190/1.3477966

Meek, R., Woller, K., George, M., Hull, R., Bello, H., & Wagner, J. (2017). Time-lapse imaging of a hydraulic stimulation using 4D vertical seismic profiles and fiber optics in the Midland Basin. *Unconventional Resources Technology Conference, Austin, Texas, 24–26 July 2017*, 3075–3082. https://doi.org/10.15530/urtec-2017-2695394

Meier, U., Shapiro, N. M., & Brenguier, F. (2010). Detecting seasonal variations in seismic velocities within Los Angeles basin from correlations of ambient seismic noise. *Geophysical Journal International*, *181*(2), 985–996. https://doi.org/10.1111/j.1365-246X.2010.04550.x

Meng, X., Chen, H., Niu, F., Tang, Y., Yin, C., & Wu, F. (2018). Microseismic monitoring of stimulating shale gas reservoir in SW China: 1. An improved matching and locating technique for downhole monitoring. *Journal of Geophysical Research: Solid Earth*, *123*, 1643–1658. https://doi.org/10.1002/2017JB014488

Mordret, A., Shapiro, N. M., & Singh, S. (2014). Seismic noise-based time-lapse monitoring of the Valhall overburden. *Geophysical Research Letters*, *41*, 4945–4952. https://doi.org/10.1002/2014GL060602

Niu, F., & Li, J. (2011). Component azimuths of the CEArray stations estimated from P-wave particle motion. *Earthquake Science*, *24*(1), 3–13. https://doi.org/10.1007/s11589-011-0764-8

Niu, F., Silver, P. G., Daley, T. M., Cheng, X., & Majer, E. L. (2008). Preseismic velocity changes observed from active source monitoring at the Parkfield SAFOD drill site. *Nature*, *454*(7201), 204–208. https://doi.org/10.1038/nature07111

Niu, F., Silver, P. G., Nadeau, R. M., & McEvilly, T. V. (2003). Migration of seismic scatterers associated with the 1993 Parkfield aseismic transient event. *Nature*, *426*(6966), 544–548. https://doi.org/10.1038/nature02151

Nur, A., & Simmons, G. (1969). Stress-induced velocity anisotropy in rock: An experimental study. *Journal of Geophysical Research*, *74*(27), 6667–6674. https://doi.org/10.1029/JB074i027p06667

Obermann, A., Kraft, T., Larose, E., & Wiemer, S. (2015). Potential of ambient seismic noise techniques to monitor the St. Gallen geothermal site (Switzerland). *Journal of Geophysical Research: Solid Earth*, *120*, 4301–4316. https://doi.org/10.1002/2014JB011817

Obermann, A., Planès, T., Larose, E., Sens-Schönfelder, C., & Campillo, M. (2013). Depth sensitivity of seismic coda waves to velocity perturbations in an elastic heterogeneous medium. *Geophysical Journal International*, *194*(1), 372–382. https://doi.org/10.1093/gji/ggt043

Okada, Y. (1992). Internal deformation due to shear and tensile faults in a half-space. *Bulletin of the Seismological Society of America*, *82*(2), 1018–1140.

Saade, M., Montagner, J. P., Roux, P., Cupillard, P., Durand, S., & Brenguier, F. (2015). Influence of seismic anisotropy on the cross correlation tensor: Numerical investigations. *Geophysical Journal International*, *201*(2), 595–604. https://doi.org/10.1093/gji/ggu470

Sánchez-Pastor, P., Obermann, A., Schimmel, M., Weemstra, C., Verdel, A., & Jousset, P. (2019). Short-and long-term variations in the Reykjanes geothermal reservoir from seismic noise interferometry. *Geophysical Research Letters*, *46*, 5788–5798. https://doi.org/10.1029/2019GL082352

Scholz, C. H. (1968). Microfracturing and the inelastic deformation of rock in compression. *Journal of Geophysical Research*, *73*(4), 1417–1432. https://doi.org/10.1029/JB073i004p01417

Sens-Schönfelder, C., & Larose, E. (2010). Lunar noise correlation, imaging and monitoring. *Earthquake Science*, *23*(5), 519–530. https://doi.org/10.1007/s11589-010-0750-6

Sens-Schönfelder, C., & Wegler, U. (2006). Passive image interferometry and seasonal variations of seismic velocities at Merapi Volcano, Indonesia. *Geophysical Research Letters*, *33*, L21302. https://doi.org/10.1029/2006GL027797

Shapiro, N. M., Campillo, M., Stehly, L., & Ritzwoller, M. H. (2005). High-resolution surface-wave tomography from ambient seismic noise. *Science*, *307*(5715), 1615–1618. https://doi.org/10.1126/science.1108339

Silver, P. G., Daley, T. M., Niu, F., & Majer, E. L. (2007). Active source monitoring of cross-well seismic travel time for stress-induced changes. *Bulletin of the Seismological Society of America*, *97*(1B), 281–293. https://doi.org/10.1785/0120060120

Snieder, R. (2004). Extracting the Green's function from the correlation of coda waves: A derivation based on stationary phase. *Physical Review E*, *69*(4), 046610. https://doi.org/10.1103/PhysRevE.69.046610

Snieder, R. (2006). The theory of coda wave interferometry. *Pure and Applied Geophysics*, *163*(2–3), 455–473. https://doi.org/10.1007/s00024-005-0026-6

Snieder, R., Grêt, A., Douma, H., & Scales, J. (2002). Coda wave interferometry for estimating nonlinear behavior in seismic velocity. *Science*, *295*(5563), 2253–2255. https://doi.org/10.1126/science.1070015

Tanimoto, T. (2004). The azimuthal dependence of surface wave polarization in a slightly anisotropic medium. *Geophysical Journal International*, *156*(1), 73–78. https://doi.org/10.1111/j.1365-246X.2004.02130.x

Warpinski, N., Mayerhofer, M., Davis, E., & Holley, E. (2014). Integrating fracture diagnostics for improved microseismic interpretation and stimulation modeling. *Unconventional Resources Technology Conference. 25–27*, 1518–1536. https://doi.org/10.15530/urtec-2014-1917906

Wegler, U., & Sens-Schönfelder, C. (2007). Fault zone monitoring with passive image interferometry. *Geophysical Journal of the Royal Astronomical Society*, *168*(3), 1029–1033. https://doi.org/10.1111/j.1365-246X.2006.03284.x

Yamamura, K., Sano, O., Utada, H., Takei, Y., Nakao, S., & Fukao, Y. (2003). Long-term observation of in situ seismic velocity and attenuation. *Journal of Geophysical Research*, *108*, 2317. https://doi.org/10.1029/2002JB002005

Yang, C., Niu, F., Daley, T. M., & Taira, T. A. (2018). Continuous measurement of stress-induced travel-time variations at SAFOD. *Seismological Research Letters*, *90*(1), 212–218. https://doi.org/10.1785/0220180080

Zuo, Q., Tang, Y., Niu, F., Li, G., Chen, H., Tao, K., & Chen, B. (2018). Temporal variations of near-surface anisotropy induced by hydraulic fracturing at a shale play site in Southwest China. *Journal of Geophysical Research: Solid Earth*, *123*, 8032–8044. https://doi.org/10.1029/2018JB016037